arXiv:1010.3910v2 [astro-ph.CO] 26 Oct 2010

Study of Faint Galaxies in the Field of GRB 021004

Yu. V. Baryshev,[1] I. V. Sokolov,[2] A. S. Moskvitin,[3]
T. A. Fatkhullin,[3] N. V. Nabokov,[1] and Brajesh Kumar[4, 5]
[1]*Institute of Astronomy, St. Petersburg State University,*
St. Petersburg, 28, University Ave., 198504 Russia
[2]*INASAN (Terskol Branch), 81, Tyrnyauz Ave., Elbrusskii, 361624, Russia*
[3]*Special Astrophysical Observatory of the Russian AS, Nizhnij Arkhyz 369167, Russia*
[4]*Aryabhatta Research Institute of Observational Sciences (ARIES), Manora Peak, Nainital, 263129, India*
[5]*Institut d'Astrophysique et de Géophysique,*
Université de Liège Allée du 6 Août 17, Bât B5C, 4000 Liège, Belgium

We present an analysis of BVR_cI_c observations of the field sized around $4' \times 4'$ centered at the host galaxy of the gamma-ray burst GRB 021004 with the 6-m BTA telescope of the Special Astrophysical Observatory of the Russian Academy of Sciences. We measured the magnitudes and constructed the color diagrams for 311 galaxies detected in the field (S/N>3). The differential and integral counts of galaxies up to the limit, corresponding to 28.5 (B), 28.0 (V), 27.0 (R_c), 26.5 (I_c) were computed. We compiled the galaxy catalog, consisting of 183 objects, for which the photometric redshifts up to the limiting magnitudes 26.0 (B), 25.5 (V), 25.0 (R_c), 24.5 (I_c) were determined using the HyperZ code. We then examined the radial distribution of galaxies based on the z estimates. We have built the curves expected in the case of a uniform distribution of galaxies in space, and obtained the estimates for the size and contrast of the possible super-large-scale structures, which are accessible with the observations of this type.

1. INTRODUCTION

To obtain the observational constraints on the existence of possible super-large-scale structures in the large-scale distribution of visible matter in the Universe a method of "space tomography" was earlier proposed [1–3]. To apply it, a reasonably large part of the celestial sphere needs to be covered with deep images of individual fields obtained with the 3–10 m class telescopes. Such images are characterized by a large penetration depth ($z \geq 1$) and a small area (from several square arcseconds to a few square degrees). In [1] the directions to gamma-ray bursts were proposed to be adopted as the centers of deep fields covering the celestial sphere.

About a dozen deep images were obtained in the program for optical identification of γ-ray bursts and during the study of their host galaxies with the 6-m BTA telescope of the Special Astrophysical Observatory of the Russian Academy of Sciences (SAO RAS) [4]. The results of study of several deep fields obtained with the BTA were discussed in [5, 6].

The goal of this work is to separate and study the objects in the field of GRB 021004, and to compile a catalog of distant galaxies. We demonstrate the feasibility of obtaining the constraints on the size and contrast of super-large-scale structures based on the four-band observations of deep fields with the BTA on the example of this field.

2. OBSERVATIONS AND DATA REDUCTION

2.1. Observations and Reduction

The photometric observations of the field of the host galaxy of GRB 021004 were performed with the BTA from November 29 to December 5, 2002 (see [7–9]) in the program of optical identification of gamma-ray bursts. The area was centered on the coordinates of the host galaxy $\alpha_{2000.0} = 00^h26^m54^s.69$, $\delta_{2000.0} = +18^o55'41''.3$ [10], which corresponds to the galactic latitude and longitude $b = -43^o33'41''.1$, $114^o55'01''.1$, respectively. The observations were carried out with the SCORPIO focal reducer [11], mounted in the main focus, with the 1034 × 1034 CCD chip TK1024 used as a radiation detector.

The CCD chip pixel size is 24 × 24 microns, which corresponds to the angular scale of $0.289''$ per element. We made use of broadband filters, which, combined with the spectral sensitivity of the CCD chip, implement the photometric system close to the standard Johnson-Krohn-Cousins BVR_cI_c system [12]. The total exposure time was 2600 s. (B), 3600 s. (V), 2700 s. (R_c), and 1800 s. (I_c). The observational conditions were photometric with an average image quality of 1.3 arcseconds. It was estimated as the full width at half maximum (FWHM) of the image of star-shaped objects in the field.

Initial data reduction was carried out with a standard technique applied to the CCD data, using the `ESO-MIDAS` package[1], and consisted of e-zero subtraction, division by the flat field, removal of the traces of interference in the R_c and I_c filters, removal of traces of cosmic particles. All the frames obtained in one filter were summed up. They were pre-reduced to the reference frame using a set of reference objects: the geometric transformation (the shift, rotation, scaling) was computed. We commonly used 7–15 reference objects. Star-shaped objects were used for a more accurate conversion, which helped achieve the accuracy of 0.2–0.5 CCD chip elements while computing the shift.

The combined frames were identically oriented, and reduced to a common coordinate system. The size of the overlap region of the combined images in all the filters amounted to about $4' \times 4'$. The astrometric calibration of the reduced frames was done with the use of the *wcstools* and

---

[1] the MIDAS (Munich Image Data Analysis System) package is distributed and supported by the European Southern Observatory

ds9 codes, and employing the USNO-B1.0 catalog [13].

The reference stars should meet the following criteria to be calibrated relative to the global coordinate system:

- their centers should be easily determined;
- their images should not reach saturation;
- they should not be too weak, so that their positions are not distorted by the background noise;
- own motion must be absent or minimal, as the images of the studied region and the images of reference stars from the catalogs are obtained at different epochs, between which the stars can significantly shift;
- they should not overlap.

To perform the calibrations we selected six reference stars. The astrometry error amounted to $0''.2$. Further, the frames that were reduced and calibrated relative to the global coordinate system were superimposed using the ALIGN/IMAGE and REBIN/ROTATE procedures of the `ESO-MIDAS` package, hence determining the region common to all frames where the objects of study were then searched for (see Fig. 1).

2.2. Object Separation and Photometry

The software package `SExtractor` [14] was used for the search and photometry of a large number of objects in the field. The <STAR CLASS> parameter of the `SExtractor` package served as a criterion for separating the star-shaped and extended objects. The object is considered star-shaped if the <STAR CLASS> parameter for it is greater than 0.7.

The package allows measurements of several magnitude types:

- *The isophote magnitude* is determined as the integral flux over the region with an intensity above a specified limit;
- *The corrected isophote magnitude* is determined in the following manner: the profile of the object is approximated by a two-dimensional Gaussian, and, proceeding from the parameters found, the corresponding correction is applied to the isophote value;
- *The automatic magnitude,* Kron [15] has demonstrated that in the objects with star formation, power-law and exponential profiles, reduced with a Gaussian, approximately 92% of the flux is enclosed in an aperture of radius kr_1, where $k \approx 2$, and $r_1 = \frac{\sum rI(r)}{\sum I(r)}$. The `SExtractor` package estimates the elliptical aperture with the major axes of ϵkr_1 and kr_1/ϵ, where ϵ stands for ellipticity. The automatic value is determined as the magnitude measured in such an aperture;
- *The aperture magnitude* is estimated as a

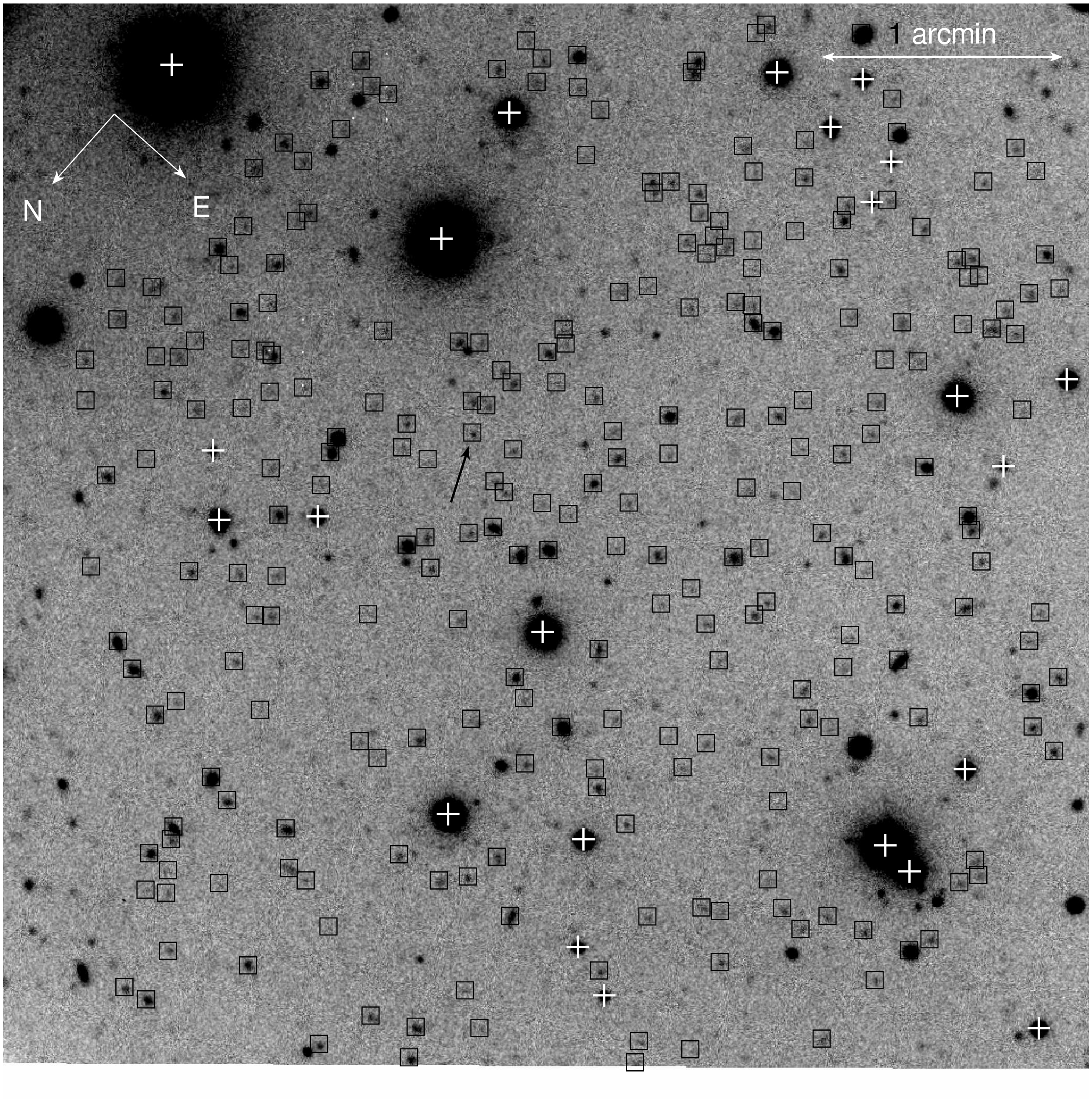

Figure 1. The objects detected in four filters (the galaxies are enclosed by the squares, the star-shaped objects are marked by crosses). The black arrow points to the host galaxy.

magnitude, measured in the circular aperture defined by the user.

The total magnitude is equal to the automatic magnitude, unless the corresponding aperture of the object captures the neighboring object, varying the magnitude by more than 0.1^m. Otherwise, the corrected isophote magnitude is used.

Background construction is a very important procedure for the automatic object search. This is why it was monitored visually. The approximated background was checked for the absence of structures around bright objects, and sharp fluctuations on small scales (below 5–7 FWHM).

The 3σ excess of intensity over the background was selected as a detection limit, where σ stands for the background fluctuations. A detected candidate is considered a real object if it occupies at least four adjacent elements of the CCD chip. In total we discovered 637, 771, 1169 and 615 objects in the B, V, R_c and I_c bands, respectively. The isophote, aperture and full magnitudes were measured for all the catalogue objects.

The object's magnitude in the instrumental system is calculated as follows:

$$m_{aper} = -2.5 \times \log(\frac{F}{T_{exp}}) - \frac{k}{\cos Z}, \qquad (1)$$

where F is the flux from the object (in counts) at a given aperture, T_{exp} is the exposure time (in seconds), k denotes the atmospheric extinction coefficient, and Z is the zenith distance (in degrees). The atmospheric extinction coefficients were adopted from [16] and are, respectively, $k_B = 0.34$, $k_V = 0.21$, $k_{R_c} = 0.15$ and $k_{I_c} = 0.1$ magnitudes. To calculate the instrumental value in the case of star-shaped objects the so-called finite-aperture corrections were used. Then the expression for the total magnitude is written as

$$m = m_{aper} - \delta m,$$

where m_{aper} is the magnitude, determined from the expression (1) and δm is the finite-aperture correction, estimated from the growth curves for the brightest star-shaped objects in the field.

To determine the magnitude measurement errors the signal-to-noise ratio was computed

$$\frac{S}{N} = \frac{F}{\sqrt{F/g + A \times \sigma^2}},$$

where F is the flux from the object (in counts) at a given aperture, g is the transformation quantum (electrons per count), A is the number of elements in the aperture and σ^2 is the background dispersion (in counts). Then the error is calculated as follows:

$$\sigma_m = \frac{2.5}{\ln 10} \times \frac{\sigma_F}{F} = \frac{2.5}{\ln 10} \times \frac{1}{S/N}.$$

The photometric calibration was performed using secondary standards adopted from [17], for which the difference between the instrumental and standard values in each band was calculated. Their averaged values were taken as zero points. The zero-point errors amounted to $0.01 - 0.02^m$

Photometry of a large number of objects in the field allowed us to determine the limiting magnitude. The detection limit was set as the average magnitude of objects with S/N= 3, 28.0, 27.5, 27.0 and 26.0 in the B, V, R_c and I_c filters, respectively.

3. PHOTOMETRIC REDSHIFT MEASUREMENTS

Measuring spectroscopic redshifts for hundreds of faint objects in deep fields is a rather complicated and laborious process which requires a lot of observational time. However, there exist many tasks for which the photometric redshift estimates based on multicolor photometry are quite acceptable. The accuracy of such estimates is about 10%, however, this is often enough for statistical studies of the properties of distant objects.

The photometric redshifts of galaxies detected in the field of the host galaxy GRB 021004 from the data of broadband observations performed with the BTA were measured using the HyperZ [18] software package.

The HyperZ package input data includes: the BVR_cI_c values and the errors thereof, absorption in our Galaxy, the cosmological model parameters, spectral energy distribution of different types of galaxies, diverse extinction laws in the galaxies. The absorption in our Galaxy was adopted at $E(B-V)=0.025$ according to the dust maps from [19]. We used a cosmological model with $H_0 = 70$ km/s/Mpc, $\Omega_M = 0.3$ and $\Omega_\Lambda = 0.7$. The spectral energy distributions were adopted from the library of model spectra (the templates, template spectra), provided by the HyperZ package. The models differ by the nature of star formation. This is either a constant rate of star formation, an exponential decline, or an initial burst of star formation in the form of a delta function.

To estimate the photometric redshifts of galaxies we have to take into account the peculiarities of internal laws of extinction and absorption in the line of sight, as it significantly affects the result. We considered the alternate versions presented in the HyperZ package. This is the same law of absorption, similar to the laws for the Large and Small Magellanic Clouds in our Galaxy, and the law of extinction for the galaxies with star formation. These laws differ by the slope of curves in the far ultraviolet region and, more importantly, by the presence or absence of the graphite absorption band at 2200Å. The absorption range was assigned as equal and amounted to $A_V = 0.0 - 3.0$ mag. with the step of 0.3. The redshift was registered in the range of $z = 0.0 - 5.0$ with the step of 0.1.

Apart from measuring the redshift we estimated other parameters of the galaxies (see Table 1.). For example, the spectral type of a given galaxy was determined based on the similarities of energy distribution in the object's spectrum to one of the theoretical template spectra.

4. RESULTS

4.1. Catalogue of Discovered Objects

From the list of objects, discovered in the deep field, we selected those with the probability to have their redshifts coincide with the computed values greater than or equal to 0.9. The final catalog contains 183 extragalactic objects within the redshift range from 0.05 to 3.8 (Fig. 1 and Table 1).

Table 1. The catalog of objects, Part 1. # is the object number; RA and Dec are the equatorial coordinates at the epoch 2000.0; R mag +/- Error is the R-band magnitude; A and B are the semi major and semi minor axes of the ellipsis, describing the object; Θ denotes the slope of the object's major axis to the horizontal axis of the frame; Ellip is the ellipticity of the object; Z is the photometric redshift; % is the probability of redshift measurement from the data available; Type denotes the galaxy type. Due to a technical error, one object appears twice in the catalog (objects # 173 and # 180 are marked with an asterisk). This error does not affect the main results of this paper

#	RA	Dec	R mag	Error	A	B	Θ	Ellip	Z	%	Type
1	6.748988	18.96673	22.98	0.06	2.077	2.017	–19.27	0.029	2.45	99.990	Burst
2	6.754534	18.96330	22.45	0.06	2.429	2.077	–46.64	0.145	0.42	95.520	Burst
3	6.767069	18.95318	23.90	0.13	2.171	1.303	49.06	0.400	0.41	99.930	Sb
4	6.729459	18.88992	19.60	0.05	4.553	3.624	29.35	0.204	0.35	99.440	E
5	6.736205	18.89336	20.19	0.05	3.702	3.484	3.76	0.059	0.45	98.920	Burst
6	6.705855	18.91868	23.85	0.10	1.724	1.562	–37.67	0.094	1.75	99.800	Burst
7	6.734323	18.89186	23.95	0.10	1.628	1.547	7.16	0.050	0.65	100.000	Im
8	6.731594	18.89799	24.01	0.10	1.879	1.260	52.26	0.330	0.53	99.970	Burst
9	6.743403	18.88873	22.93	0.08	2.668	1.861	–88.43	0.303	0.73	98.500	Burst
10	6.702297	18.91715	22.08	0.05	2.635	2.464	31.56	0.065	0.62	99.970	E
11	6.728497	18.90112	23.28	0.08	2.503	1.779	52.79	0.289	0.73	99.830	E
12	6.705405	18.91507	23.11	0.08	2.483	2.093	–17.57	0.157	1.46	98.870	Burst
13	6.736987	18.89948	23.44	0.08	2.118	1.452	–87.19	0.315	2.78	99.820	Sd
14	6.737479	18.90041	21.93	0.05	2.723	2.447	48.22	0.101	0.44	96.280	Burst
15	6.742126	18.89711	23.49	0.11	2.220	1.719	20.11	0.226	0.41	99.780	Burst
16	6.726112	18.90621	21.96	0.05	2.498	2.307	–26.04	0.076	0.35	98.190	Burst
17	6.725135	18.90713	23.23	0.09	2.508	1.875	–30.05	0.253	1.72	99.920	Burst
18	6.729369	18.90655	24.26	0.11	1.472	1.303	59.90	0.115	2.19	94.430	Burst
19	6.731282	18.90706	23.10	0.07	2.320	1.569	–42.97	0.324	0.43	99.940	Burst
20	6.732459	18.90715	21.09	0.05	5.466	2.463	–12.78	0.549	0.71	90.680	Burst
21	6.733622	18.90553	24.04	0.10	1.739	1.406	–2.71	0.192	2.10	87.200	Burst
22	6.730179	18.90870	22.98	0.07	2.695	2.272	80.49	0.157	3.30	99.990	Burst
23	6.704854	18.93039	20.34	0.05	4.999	3.596	35.40	0.281	0.52	94.570	E
24	6.745641	18.89719	23.67	0.12	2.008	1.888	–33.24	0.060	2.05	98.080	Burst
25	6.708762	18.92858	20.82	0.05	4.922	2.445	39.95	0.503	0.60	94.970	Burst
26	6.746276	18.89642	23.08	0.10	2.590	1.733	–22.66	0.331	1.20	99.940	S0

Table 1. (Contd.)

#	RA	Dec	R mag	Error	A	B	Θ	Ellip	Z	%	Type
27	6.705244	18.92806	22.28	0.06	2.994	2.168	–45.99	0.276	0.56	99.880	Burst
28	6.739671	18.90300	22.61	0.07	2.427	1.662	–75.29	0.315	1.10	99.980	E
29	6.715098	18.90405	21.00	0.05	3.372	2.312	38.00	0.314	0.46	99.500	Burst
30	6.721831	18.89889	22.05	0.05	2.541	2.317	–37.56	0.088	0.71	99.920	Im
31	6.735670	18.90948	23.75	0.10	2.608	1.177	–38.20	0.549	1.88	93.270	Burst
32	6.709185	18.93276	20.69	0.05	3.152	2.578	44.84	0.182	0.55	98.720	Burst
33	6.733432	18.91188	24.07	0.10	1.466	1.173	–48.54	0.200	0.94	99.930	Burst
34	6.737649	18.90976	21.04	0.05	3.455	2.344	–63.99	0.321	0.40	99.620	Sa
35	6.745690	18.90291	23.04	0.08	3.301	1.889	–49.71	0.428	2.26	97.310	Burst
36	6.722170	18.89967	21.41	0.05	3.790	2.736	–65.25	0.278	1.15	99.930	S0
37	6.705767	18.93597	24.23	0.13	1.585	1.556	6.20	0.018	1.78	99.090	Burst
38	6.750864	18.89911	21.84	0.05	3.196	2.428	45.59	0.240	0.23	93.710	E
39	6.739073	18.90928	21.16	0.05	3.426	2.850	–48.73	0.168	0.41	99.380	Sa
40	6.722549	18.92421	21.23	0.05	2.826	2.562	–34.01	0.093	0.41	99.950	E
41	6.712472	18.93355	22.06	0.05	4.627	2.348	–63.39	0.492	0.44	96.490	Burst
42	6.713016	18.93348	22.05	0.05	2.492	1.988	–46.21	0.202	1.05	99.630	Burst
43	6.727865	18.92069	21.44	0.05	2.714	2.082	–51.35	0.233	0.55	99.070	E
44	6.711030	18.93460	24.37	0.12	1.741	1.073	–50.70	0.384	0.97	99.960	S0
45	6.726254	18.92374	22.85	0.06	2.431	1.776	–53.73	0.269	1.15	99.900	Burst
46	6.727385	18.92389	22.25	0.06	2.658	2.140	–23.10	0.195	0.66	99.550	Sc
47	6.703103	18.94228	23.81	0.12	2.020	1.433	–82.58	0.291	3.49	96.700	Burst
48	6.716295	18.93372	23.95	0.10	1.801	1.482	–23.89	0.177	0.22	99.230	Burst
49	6.732539	18.92081	23.71	0.12	2.223	1.170	1.64	0.474	1.92	98.830	Burst
50	6.726122	18.92666	22.75	0.07	2.874	1.953	–77.94	0.321	1.25	99.590	Burst
51	6.727129	18.92623	23.80	0.14	1.660	1.236	–55.46	0.256	1.59	99.950	Burst
52	6.705105	18.94435	23.35	0.09	1.844	1.740	–18.47	0.056	0.50	99.910	E
53	6.711551	18.93976	23.15	0.10	2.301	1.877	–45.06	0.184	0.61	99.800	Im
54	6.737527	18.91839	21.25	0.05	3.041	2.554	30.97	0.160	0.10	99.950	Burst
55	6.713956	18.93758	24.75	0.16	2.062	0.819	–55.35	0.603	1.93	99.360	Burst
56	6.743444	18.91343	22.97	0.09	2.417	1.977	57.70	0.182	0.50	99.980	S0
57	6.741271	18.91543	23.00	0.08	2.151	1.976	19.49	0.081	1.03	100.000	Burst
58	6.720520	18.93474	20.29	0.05	3.587	3.363	–32.56	0.063	2.23	99.250	Burst
59	6.720910	18.93579	21.33	0.05	2.852	2.724	–9.52	0.045	0.45	99.980	Im
60	6.724590	18.93225	24.55	0.13	1.306	1.185	–3.71	0.092	1.09	99.960	E

Table 1. (Contd.)

#	RA	Dec	R mag	Error	A	B	Θ	Ellip	Z	%	Type
61	6.730726	18.92726	23.36	0.10	2.335	1.788	21.24	0.234	0.60	100.000	Sc
62	6.748846	18.91243	22.85	0.07	2.715	2.155	–52.13	0.206	0.64	100.000	E
63	6.736760	18.92292	22.22	0.06	3.263	2.453	70.60	0.248	0.39	99.560	Burst
64	6.753927	18.90931	21.29	0.05	3.308	2.441	78.50	0.262	0.35	90.210	E
65	6.726554	18.93169	24.46	0.14	1.761	1.341	54.14	0.238	0.57	99.000	Burst
66	6.711230	18.94458	25.11	0.19	1.336	0.746	16.83	0.442	0.51	100.000	Burst
67	6.709861	18.94726	22.03	0.06	3.300	2.313	50.36	0.299	0.46	99.740	S0
68	6.736685	18.92534	21.77	0.05	2.658	2.189	–24.78	0.177	0.41	95.920	Sa
69	6.722001	18.93792	24.14	0.17	1.721	0.962	86.30	0.441	2.81	99.990	Burst
70	6.732282	18.92990	24.12	0.15	1.536	1.053	–76.79	0.314	0.35	86.370	Burst
71	6.758679	18.90984	20.60	0.05	3.836	3.334	33.44	0.131	0.40	86.390	Burst
72	6.721132	18.94138	20.47	0.05	3.866	3.689	–21.19	0.046	0.29	99.980	E
73	6.733374	18.93218	21.76	0.05	3.137	1.919	59.43	0.388	1.09	98.950	E
74	6.736860	18.92805	24.15	0.10	1.332	1.287	–10.30	0.034	0.64	99.650	Burst
75	6.732345	18.93360	23.11	0.07	2.416	1.519	24.85	0.371	0.35	99.910	S0
76	6.730218	18.93581	22.46	0.06	2.979	1.954	–21.09	0.344	0.44	98.440	E
77	6.729551	18.93704	20.21	0.05	3.677	3.230	36.52	0.122	0.44	98.650	E
78	6.737521	18.93082	20.05	0.05	3.210	2.526	51.20	0.213	0.38	91.080	Burst
79	6.736118	18.93245	21.37	0.05	3.834	2.793	–35.86	0.272	2.97	99.920	Burst
80	6.747920	18.92270	20.59	0.05	4.587	3.421	22.91	0.254	0.63	97.280	Burst
81	6.743696	18.92608	22.59	0.06	2.449	2.312	–10.35	0.056	0.64	99.850	S0
82	6.741006	18.92750	22.64	0.06	2.975	2.208	–66.72	0.258	0.50	96.220	Burst
83	6.731962	18.93714	22.67	0.06	2.493	1.749	37.32	0.298	0.35	96.560	Burst
84	6.753860	18.91760	21.42	0.05	3.386	2.719	–46.55	0.197	0.40	87.660	Burst
85	6.721753	18.94624	23.28	0.08	2.316	1.664	–50.62	0.282	0.65	99.490	E
86	6.719014	18.94839	21.16	0.05	2.837	2.675	–32.09	0.057	0.41	99.650	Burst
87	6.751827	18.92470	23.26	0.09	2.001	1.508	44.36	0.247	0.41	92.240	Burst
88	6.724735	18.94761	23.39	0.10	2.556	1.541	–18.54	0.397	0.51	99.980	Burst
89	6.749628	18.92740	23.03	0.08	2.284	1.739	–34.22	0.239	0.58	100.000	Burst
90	6.759024	18.91769	22.36	0.06	2.469	1.848	–0.08	0.251	0.79	99.990	Burst
91	6.718533	18.95525	21.09	0.05	3.802	2.299	–47.04	0.395	1.04	99.790	E
92	6.768041	18.91343	22.45	0.06	3.135	2.103	51.00	0.329	0.56	97.040	E
93	6.745049	18.93361	21.86	0.05	4.577	2.252	–37.72	0.508	2.41	89.890	Burst
94	6.761848	18.92041	20.23	0.05	5.429	2.674	–3.17	0.508	0.24	99.590	E

Table 1. (Contd.)

#	RA	Dec	R mag	Error	A	B	Θ	Ellip	Z	%	Type
95	6.725812	18.95096	23.29	0.10	1.982	1.717	14.27	0.134	0.46	99.850	Burst
96	6.762870	18.91469	22.26	0.06	4.744	2.267	18.97	0.522	0.79	99.990	Burst
97	6.751862	18.92347	23.80	0.10	1.719	1.446	27.85	0.159	0.98	99.830	Burst
98	6.720642	18.95601	21.54	0.05	4.891	2.665	77.86	0.455	0.80	98.490	E
99	6.741830	18.93889	20.73	0.05	3.182	3.089	–19.42	0.029	0.35	98.320	E
100	6.771370	18.91395	22.54	0.06	2.699	2.033	–79.96	0.247	0.30	99.960	S0
101	6.770688	18.91605	20.05	0.05	5.174	3.112	81.96	0.399	0.14	88.850	Burst
102	6.758063	18.92635	23.57	0.10	2.783	1.709	–23.73	0.386	1.29	99.750	E
103	6.743377	18.93955	24.37	0.13	1.752	1.250	–21.71	0.286	2.27	95.530	Sb
104	6.724585	18.95566	23.63	0.09	1.850	1.632	57.80	0.118	0.45	99.490	Burst
105	6.724108	18.95733	21.32	0.05	3.735	2.886	–53.47	0.227	0.41	99.180	Sb
106	6.765739	18.92245	23.42	0.08	1.863	1.733	6.12	0.070	3.04	99.180	Burst
107	6.749199	18.93657	23.25	0.07	2.036	1.678	34.36	0.176	0.71	99.830	E
108	6.772387	18.91769	22.31	0.06	2.811	2.307	–12.73	0.179	0.84	99.850	Burst
109	6.741495	18.94304	22.15	0.05	3.146	2.197	–26.56	0.302	0.57	97.760	E
110	6.746771	18.93933	19.63	0.05	4.419	3.544	–59.63	0.198	0.10	89.820	Burst
111	6.761366	18.92702	24.74	0.16	1.605	1.169	38.40	0.272	2.33	99.980	S0
112	6.763813	18.92675	18.62	0.05	4.689	4.309	–6.05	0.081	2.01	99.990	Burst
113	6.753056	18.93486	24.94	0.16	1.227	0.938	–34.79	0.235	2.76	94.010	Sd
114	6.755443	18.93353	23.96	0.14	1.414	1.348	–24.95	0.046	1.44	99.910	Burst
115	6.736525	18.94930	24.59	0.13	1.333	1.177	–58.65	0.117	2.09	99.950	E
116	6.774732	18.91794	22.20	0.05	2.536	1.979	–19.45	0.220	0.35	99.750	E
117	6.755332	18.93582	23.94	0.15	1.607	1.113	–67.05	0.307	1.03	99.760	E
118	6.750640	18.93991	23.59	0.09	2.627	1.381	10.56	0.474	1.19	99.680	Sa
119	6.730174	18.95795	21.13	0.05	3.576	2.819	–27.46	0.212	2.45	99.990	E
120	6.759603	18.93127	23.60	0.09	2.861	1.424	65.14	0.502	2.45	100.000	Burst
121	6.731014	18.96300	23.05	0.07	2.313	2.155	41.70	0.068	1.00	99.970	Burst
122	6.751646	18.94078	22.00	0.06	2.762	2.264	–62.94	0.180	0.36	99.470	Burst
123	6.730519	18.96472	21.78	0.05	2.432	2.290	36.43	0.058	0.30	98.730	S0
124	6.749580	18.94896	21.26	0.05	2.786	2.548	–24.11	0.085	0.05	99.980	E
125	6.744153	18.95331	23.28	0.08	2.233	1.624	–38.00	0.273	2.27	96.730	Burst
126	6.736730	18.95718	21.41	0.05	3.700	2.580	48.97	0.303	0.10	99.990	Im
127	6.738836	18.95907	23.13	0.09	3.987	1.476	58.88	0.630	1.34	91.000	Burst
128	6.776626	18.92780	23.46	0.08	2.024	1.731	41.15	0.145	2.51	99.960	Burst

Table 1. (Contd.)

#	RA	Dec	R mag	Error	A	B	Θ	Ellip	Z	%	Type
129	6.747582	18.95283	22.75	0.07	2.287	1.997	29.62	0.126	1.82	88.150	Burst
130	6.765412	18.93769	23.46	0.12	2.501	1.399	−43.17	0.440	2.26	99.770	Burst
131	6.733354	18.96597	23.83	0.11	2.314	1.430	−50.28	0.382	0.05	99.990	Sc
132	6.732174	18.95842	22.65	0.07	2.542	2.141	50.06	0.158	2.09	99.990	Burst
133	6.767573	18.93849	22.83	0.07	2.385	1.965	−45.93	0.176	0.56	99.960	Sa
134	6.760662	18.94512	23.96	0.13	1.723	1.167	−49.25	0.323	2.63	99.180	Sa
135	6.730542	18.96223	21.67	0.05	4.197	1.976	−80.87	0.529	0.75	99.970	Sb
136	6.754972	18.94135	24.19	0.11	1.639	1.287	−12.54	0.215	1.98	99.640	Burst
137	6.776520	18.93486	20.06	0.05	3.848	3.395	−4.38	0.118	2.34	98.240	Burst
138	6.736278	18.96887	23.39	0.12	2.524	1.401	−82.57	0.445	0.35	99.830	Burst
139	6.766796	18.94414	22.78	0.07	2.243	2.024	33.94	0.098	0.45	99.930	S0
140	6.723733	18.89472	23.93	0.10	2.001	1.431	−69.78	0.285	2.27	98.600	Burst
141	6.760657	18.95011	23.14	0.09	2.117	1.727	−50.93	0.184	1.66	91.760	Burst
142	6.737427	18.97238	20.36	0.05	3.984	2.893	−86.99	0.274	0.39	92.300	Burst
143	6.750421	18.96291	22.42	0.06	2.742	2.217	66.55	0.191	0.39	98.010	Burst
144	6.753414	18.96141	22.71	0.06	2.557	1.750	53.68	0.316	2.22	97.480	Burst
145	6.752117	18.92868	24.53	0.19	1.629	0.973	2.74	0.403	1.34	100.000	Sc
146	6.758030	18.92137	23.78	0.13	1.868	1.380	−30.13	0.261	0.29	99.880	Burst
147	6.759220	18.92332	23.60	0.09	1.826	1.556	32.26	0.148	3.69	99.790	Burst
148	6.769590	18.93874	23.70	0.12	1.835	1.429	−5.32	0.221	2.07	99.930	Burst
149	6.769437	18.94998	24.28	0.14	1.103	0.501	89.53	0.546	2.95	90.880	Burst
150	6.738302	18.94934	23.63	0.10	2.680	1.952	−25.90	0.272	3.31	99.950	E
151	6.723996	18.94461	24.10	0.13	2.223	1.609	−29.12	0.276	2.40	95.140	Sc
152	6.730829	18.94240	24.24	0.16	1.487	1.022	44.88	0.313	0.63	100.000	Sa
153	6.740344	18.95894	24.36	0.17	2.201	1.406	−69.58	0.361	2.69	96.410	Sd
154	6.743816	18.96026	24.04	0.17	1.677	1.430	38.54	0.147	3.54	99.900	Sa
155	6.732366	18.96473	23.51	0.13	1.640	1.435	−47.48	0.125	3.80	87.610	E
156	6.743285	18.89193	23.19	0.11	2.120	1.636	60.39	0.228	0.50	99.270	Burst
157	6.745655	18.88898	23.67	0.11	2.148	1.379	−16.61	0.358	3.60	99.990	Burst
158	6.747603	18.89697	24.03	0.16	1.605	1.014	−44.01	0.368	1.39	99.590	Burst
159	6.735456	18.90313	24.66	0.18	1.423	1.141	35.47	0.198	1.63	96.560	Burst
160	6.730319	18.90195	24.90	0.16	1.918	0.701	54.44	0.635	1.53	99.990	E
161	6.730860	18.90607	24.00	0.16	1.525	1.201	20.44	0.212	1.66	96.430	Burst
162	6.731735	18.90833	24.04	0.11	1.973	1.415	−18.91	0.283	2.26	99.990	Burst

Table 1. (Contd.)

#	RA	Dec	R mag	Error	A	B	Θ	Ellip	Z	%	Type
163	6.742588	18.90509	22.45	0.06	3.378	1.967	11.62	0.418	0.35	99.020	Burst
164	6.744093	18.91145	24.70	0.14	1.391	1.059	47.77	0.239	2.24	100.000	Burst
165	6.749406	18.91006	23.97	0.13	1.804	1.208	–43.74	0.330	2.63	99.990	Im
166	6.747906	18.91661	23.93	0.11	1.999	1.173	35.16	0.413	0.54	93.320	Burst
167	6.739581	18.92470	23.49	0.10	2.237	1.546	–42.31	0.309	0.43	89.410	Burst
168	6.739374	18.92036	24.56	0.14	1.787	1.020	–14.99	0.429	2.67	97.450	S0
169	6.735257	18.92176	23.79	0.12	1.426	1.284	20.96	0.100	1.68	99.990	Burst
170	6.730132	18.91267	23.93	0.16	3.339	0.867	–46.04	0.740	0.42	98.610	Burst
171	6.728870	18.91431	23.42	0.11	2.211	1.813	–49.87	0.180	1.29	99.670	S0
172	6.725771	18.90754	23.76	0.09	2.035	1.415	–36.30	0.304	2.09	99.720	Burst
173*	6.716690	18.90568	23.10	0.09	3.120	1.616	–72.57	0.482	0.10	99.990	Burst
174	6.703195	18.93548	20.80	0.05	4.402	3.699	34.14	0.160	0.51	85.610	Burst
175	6.708062	18.93785	23.04	0.09	3.789	1.971	–54.30	0.480	0.64	99.750	Sa
176	6.714692	18.93546	23.92	0.10	2.655	1.027	–51.73	0.613	1.12	99.990	Burst
177	6.718461	18.93935	24.08	0.11	1.873	1.334	–33.51	0.288	0.31	100.000	Burst
178	6.734882	18.92871	24.82	0.14	1.144	1.013	–47.51	0.114	2.69	100.000	Burst
179	6.729826	18.92184	25.11	0.27	1.198	0.903	–44.68	0.246	1.26	99.910	Burst
180*	6.716690	18.90568	23.10	0.09	3.120	1.616	–72.57	0.482	0.10	99.990	Burst
181	6.711601	18.90566	25.49	0.19	1.024	0.594	–86.17	0.420	1.66	98.740	E
182	6.703599	18.91426	23.16	0.09	3.002	1.722	–39.10	0.426	1.50	98.900	Sd
183	6.727688	18.92827	24.17	0.15	1.481	1.099	–19.94	0.258	2.21	99.980	E

Furthermore, for 311 field galaxies we estimated the magnitudes and errors therein in four filters, the redshifts, global coordinates for the epoch 2000.0, galaxy types (in some cases, several types fit simultaneously based on the χ^2 criterion, hence a detailed study of each object is needed), ellipticity, the stellarity index, the semi major and semi minor axes of the inscribed ellipses A and B, as well as the corresponding position angles Θ. Table 1 lists some of the above parameters for 183 galaxies with reliable estimates of photometric redshifts.

4.2. The Observed Ratios for Faint Galaxies

The compiled catalog of galaxies in the field of GRB 021004 allows us to study the observed relations between various parameters of the galaxies, and to conduct a preliminary (without redshift data) selection of objects for a more detailed investigation.

By way of example for the galaxies of this

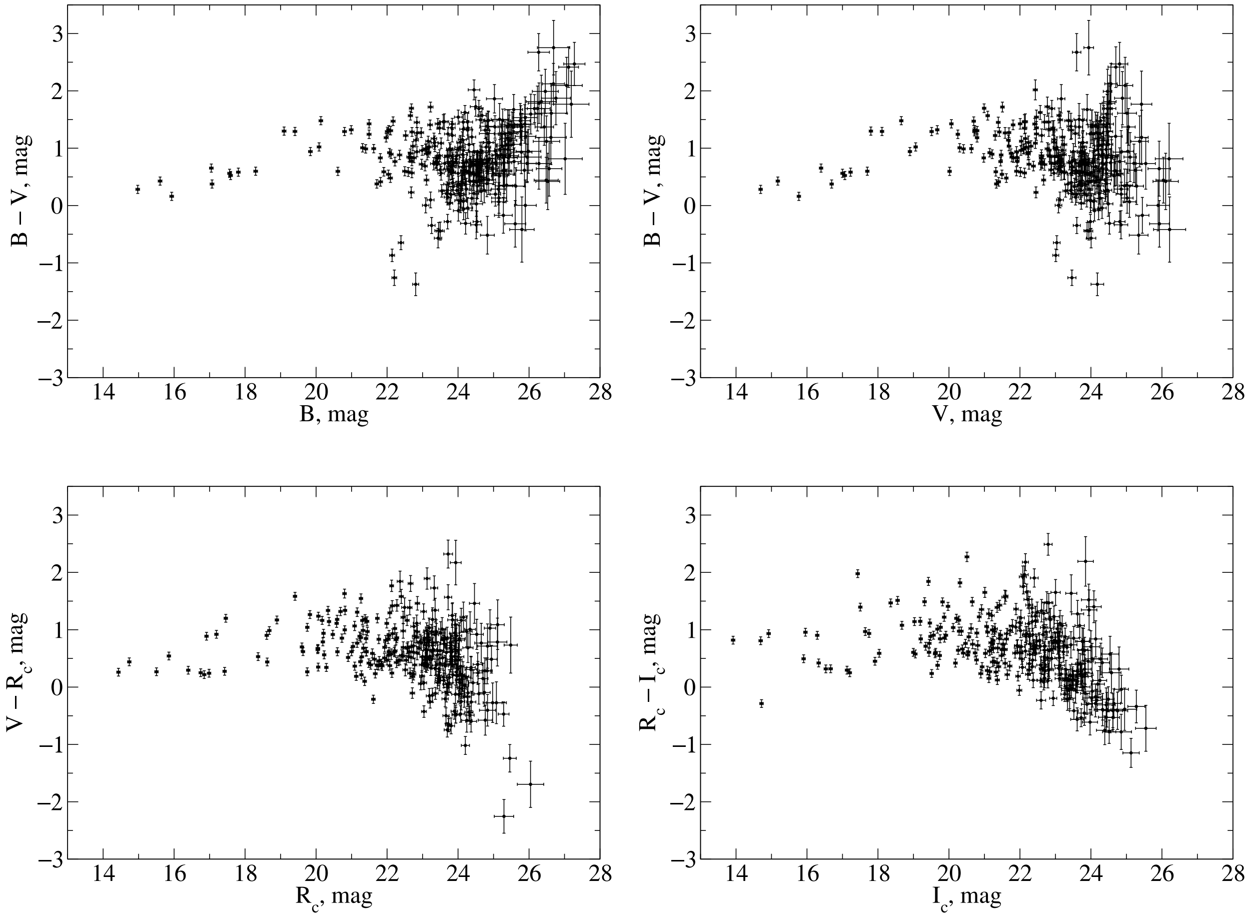

Figure 2. Color–magnitude diagrams for the discovered field galaxies.

field we constructed the color–magnitude diagrams (Fig. 2), and performed the differential and integral counts (Figs. 3 and 4).

The color indices (Fig. 2) reflect the shape of a continuous spectrum of the galaxy as a function of the observed flux. These indices can be used for planning the future detailed observations of these galaxies on other telescopes. The differential and integral counts of galaxies in this field (Figs. 3 and 4) are needed to make a comparison with the future observations of the nearby fields with the BTA and other telescopes involved in this program.

Dependencies of Apparent Values on Redshift

The obtained photometric estimates of z for the galaxies of the field of GRB 021004 allow to study both the actually observed evolution of parameters of different types of galaxies, and the evolution of the large-scale structure of the Universe in the radial direction. It should be noted that for such astrophysical tasks as the evolution of the luminosity function of different types of galaxies, identified by the HyperZ code via fitting the template continuous spectra of galaxies over broadband photometric observations, as well as for the detection of super-large-scale ir-

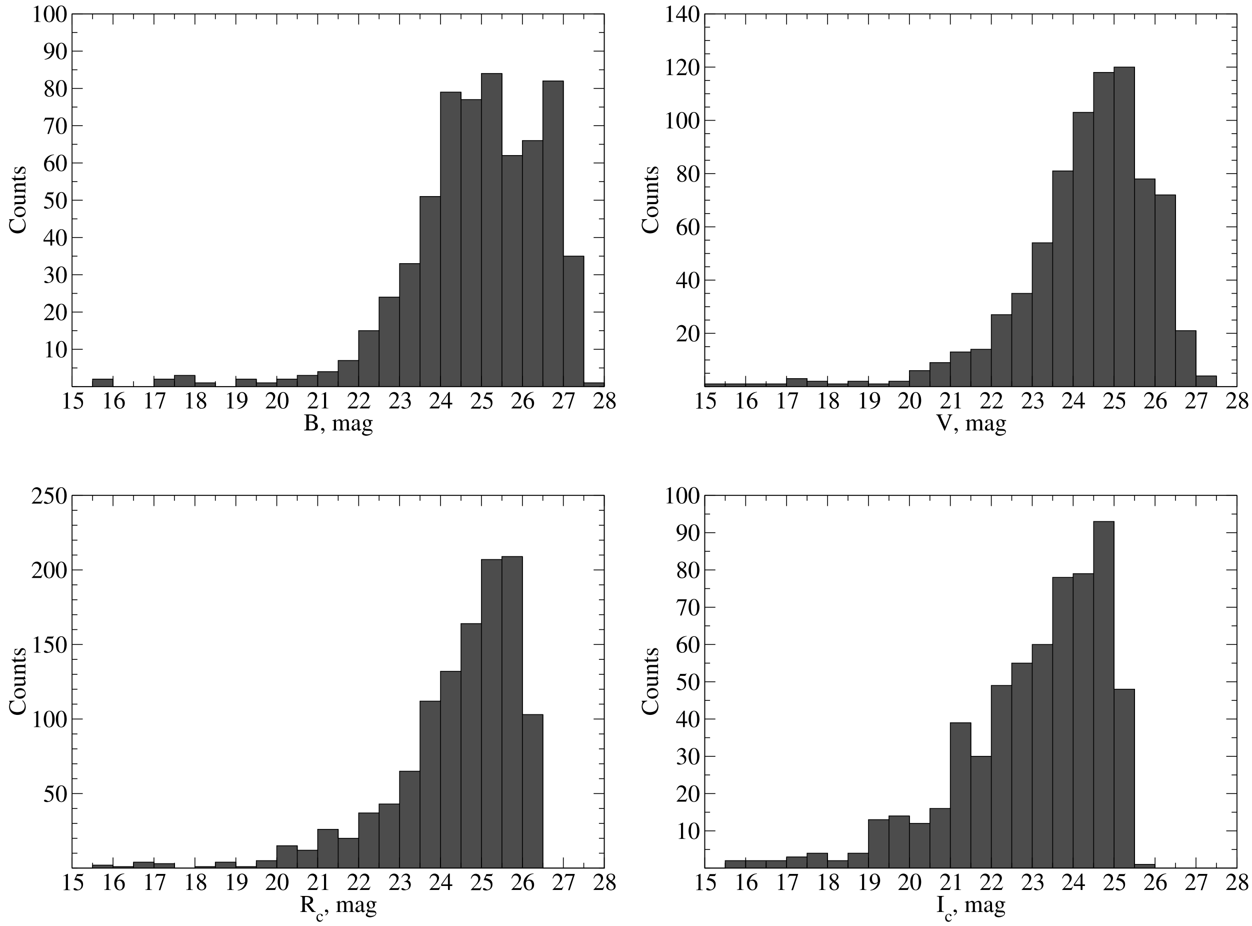

Figure 3. Differential counts of galaxies in four filters.

regularities in the spatial distribution of galaxies, the redshift estimates on the order of 10–20% are sufficient enough.

As an example, we present the dependencies of the detected objects' magnitudes on their photometric redshifts, which are presented in Fig. 5. These charts show the presence of a fairly broad luminosity function in distant galaxies, as well as the range of apparent magnitudes corresponding to a fixed redshift.

4.3. A Search for Super-Large-Scale Structures

In order to have a homogeneous distribution of galaxies in space, we anticipate a smooth distribution of redshifts. The deep surveys are magnitude–limited by the samples, where the galaxy distribution by redshift is normally approximated by the formula from [2]:

$$N_{mod}(z, \Delta z) = A z^{\alpha} e^{\left(-\frac{z}{z_0}\right)^{\beta}} \Delta z, \qquad (2)$$

where $N_{mod}(z, \Delta z)$ is the number of galaxies with redshifts in the range of $(z, z + \Delta z)$, the free parameters α, β, z_0 are found using the method of least squares, and A is the normalization parame-

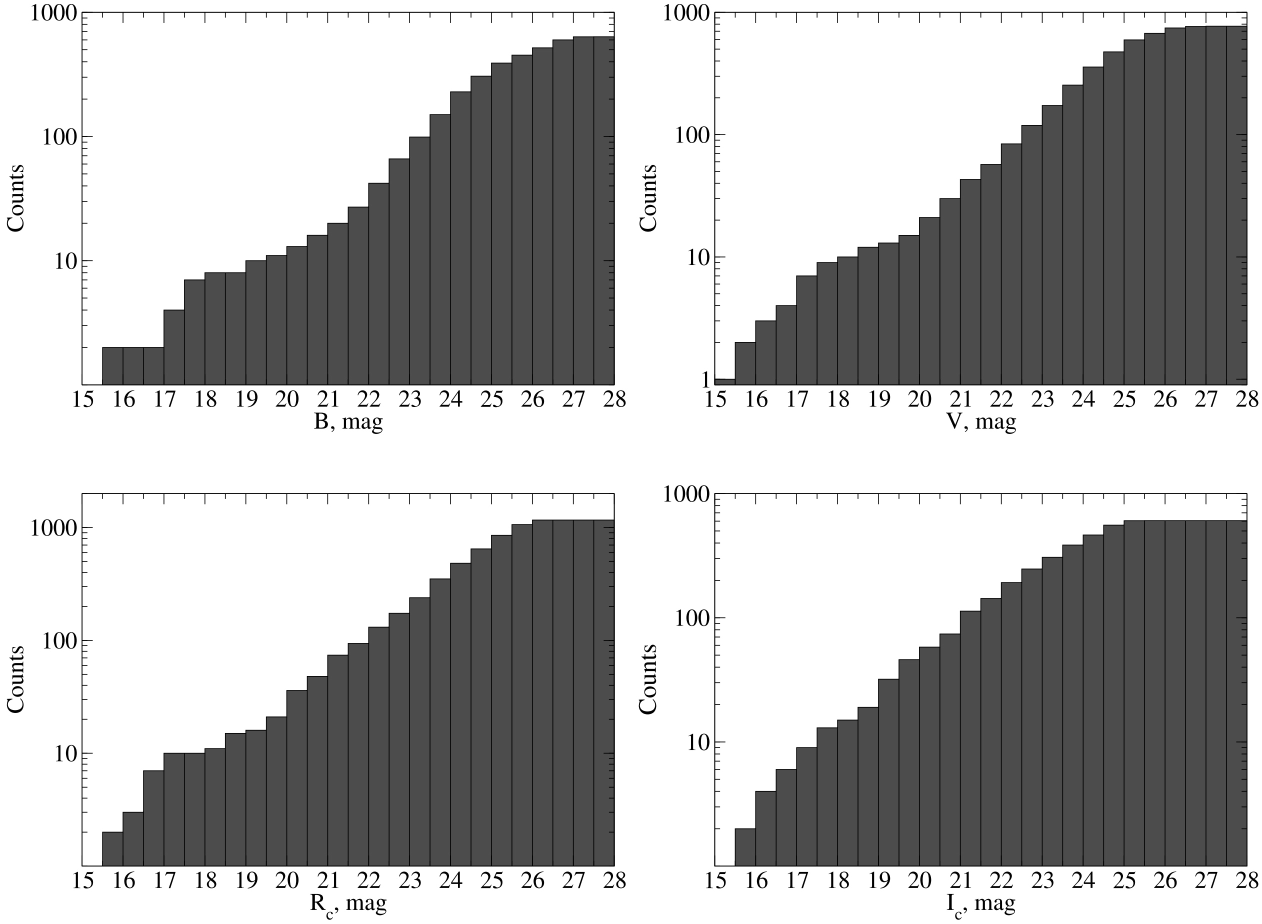

Figure 4. Integral counts of galaxies in four filters.

ter, which corresponds to the condition $\int N_{mod} = N_{total}$.

The present paper gives an analysis of the radial distribution of galaxies in increments of $\Delta z = 0.2$ and $\Delta z = 0.3$ in order to select probable regions of high and low density. Switching from $\Delta z = 0.2$ to $\Delta z = 0.3$, we identify large structures, resistant to the considered scale of Δz. The measure of deviation of the observed redshift distribution $N_{obs}(z, \Delta z)$ from the expected one $N_{mod}(z, \Delta z)$ for the given bin $(z, \Delta z)$ that we used is expressed by the formula

$$\sigma_{obs}(z, \Delta z) = \frac{\Delta N_{obs}}{N_{mod}} = \frac{N_{obs}(z, \Delta z) - \langle N \rangle}{\langle N \rangle}, \tag{3}$$

where the mean expected number of galaxies $\langle N \rangle = N_{mod}(z, \Delta z)$ is given by the formula (2). Based on the ratio (3), we isolate the regions (with number i) with an excess (Over Density Region, ODR_i) and low (Under Density Region, UDR_i) density of galaxy number relative to the Poisson level σ_p, i.e. the regions with a relative density fluctuation $\Delta N/N > +\sigma_p$ and $\Delta N/N < -\sigma_p$.

Figure 6 presents radial distributions

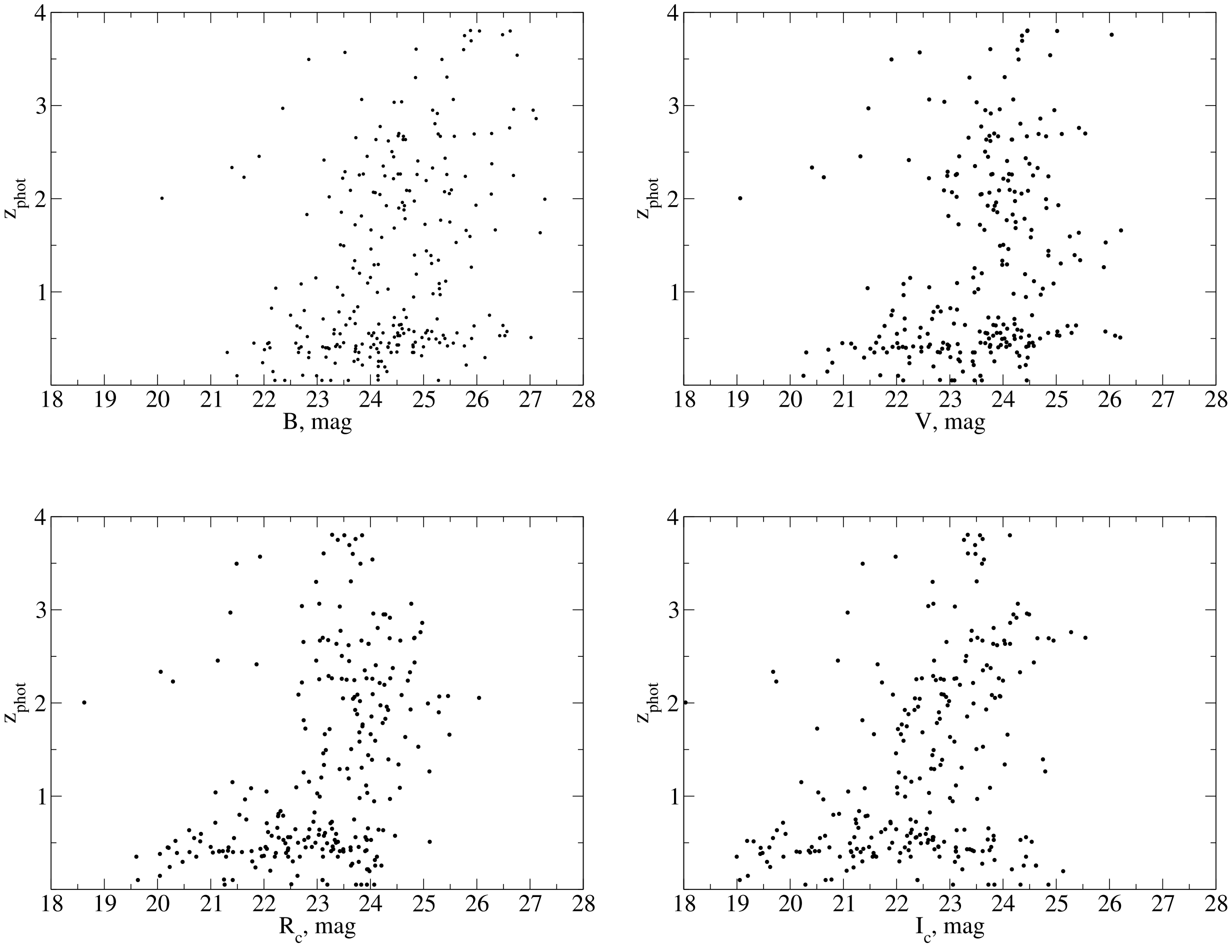

Figure 5. Magnitude–redshift diagrams for the objects discovered.

of galaxies (denoted by the dots) in the field of GRB 021004, with the bin sizes of $\Delta z = 0.2$ ($\Delta r = 600$ Mpc$/h$, $h = H/(100$ km/s/Mpc$)$) and $\Delta z = 0.3$ ($\Delta r = 900$ Mpc$/h$). The same figure has the theoretically expected distributions (the thick smooth line), plotted for a homogeneous distribution of galaxies in space, the deviations from which are caused by the Poisson fluctuations (σ_p), by the correlated structures (σ_{corr}) and by the possible systematic errors ($\sigma_{systematic}$) [2]. The coefficients of theoretical distributions for the bins $\Delta z = 0.2$ are: $\alpha = 0.63 \pm 0.30$, $z_\circ = 0.9$, $\beta = 1.27 \pm 0.30$, $A = 57.28 \pm 11.45$, and for the bins $\Delta z = 0.3$: $\alpha = 0.74 \pm 0.47$, $z_\circ = 0.9$, $\beta = 1.27 \pm 0.38$, $A = 89.71 \pm 23.47$.

Figure 7 demonstrates relative deviations of the number of galaxies from the theoretical curves in the bins $\Delta z = 0.2$ and $\Delta z = 0.3$ based on redshift. One can highlight the regions of high and low density in the graphs. Table 2 presents the regions of high and low density, as well as their sizes in the radial direction Δr, detected at the level of $\pm\sigma_p$ in the case of the radial distribution of $\Delta z = 0.3$, where $\sigma_{corr} = |\sigma_{obs} - \sigma_p|$. Note that a small number of galaxies within the

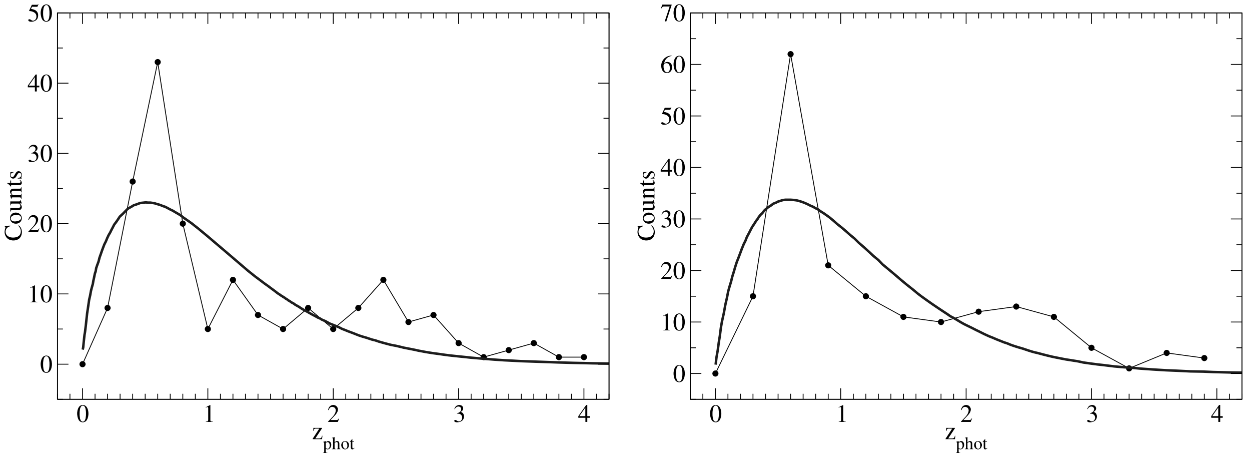

Figure 6. Radial distribution of galaxies for the bins $\Delta z = 0.2$ (left) and $\Delta z = 0.3$ (right).

range of $z > 3.5$ does not permit to assert that we indeed observe a region with an increased concentration of galaxies. The value of the detection threshold is variable, we adopted it at $\pm\sigma_p$ since this is a characteristic value of the Poisson distribution.

5. CONCLUSION

Our main objective was to study the feasibility of the "space imaging" method with the BTA in order to obtain the observational constraints on the existence of super-large structures. This technique allows to study the gigaparsec-scale structures based on the observed distributions of photometric redshifts of faint galaxies in deep fields in the adjacent areas of the celestial sphere.

As a first step, the preset work investigates the deep field sized $4' \times 4'$ around the host galaxy of the gamma-ray burst GRB 021004, obtained on the BTA with the SCORPIO focal reducer in the BVR_cI_c filters.

We have compiled a catalog of galaxies detected in the field: 183 objects with the SNR greater than 3 in each filter, and with the limiting magnitudes of 26.0 (B), 25.5 (V), 25.0 (R_c), 24.5 (I_c). This allowed us to measure the photometric redshifts of the field galaxies up to $z \approx 4$ with probability of 0.9. Here we used the Seaton's extinction law (MW).

Earlier, Nabokov and Baryshev [1] took an example of 100 gamma-ray bursts with known redshifts and showed that the radial distribution of gamma-ray bursts is consistent with radial distributions of galaxies in the other currently available deep fields. An analysis of the deep field of GRB 021004, carried out in the present paper, shows that selection of faint galaxies and construction of radial distributions in deep fields of gamma-ray bursts, reachable with the BTA, can be used with the aim of investigating the large-scale structure of the Universe on Hubble scales. In the case of absence of systematic effects in the technique of photometric redshift mea-

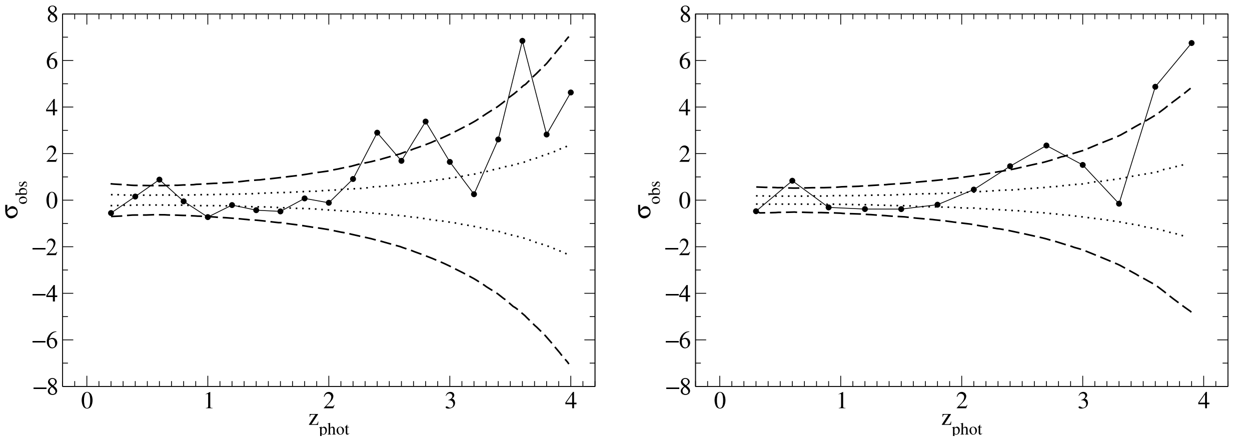

Figure 7. The observed σ_{obs} deviations and the Poisson noise σ_p (dotted lines) and $3\sigma_p$ (dashed lines) for the bins $\Delta z = 0.2$ (left) and $\Delta z = 0.3$ (right).

Table 2. The Over Density (ODR) and Under Density Regions (UDR), according to the data of the radial distribution of galaxies in the field of GRB 021004 for the bins $\Delta z = 0.3$

z_{start}	z_{finish}	Δz	Δr	σ_{corr}	Name
0.45	0.76	0.31	922	0.64	GRB021004_ODR_1
0.86	1.71	0.85	1721	0.16	GRB021004_UDR_1
2.07	3.14	1.07	1166	1.51	GRB021004_ODR_2

surement, we can assume that in the radial direction there are possible gigaparsec-scale structures with contrast equal to 50%. To estimate the size and contrast of super-large-scale structures in the tangential direction, one needs similar deep field examinations in the neighboring areas of gamma-ray bursts, as well as modeling the selection effects, which could potentially distort the observed radial distribution of distant galaxies.

ACKNOWLEDGMENTS

The authors are grateful to V. N. Komarova for the methodological assistance with the BTA data reduction, A. A. Vasilyeva for useful discussions and advice, as well as the anonymous referee for his/her comments which helped significantly improve the presentation of this paper. The work was supported by the RNP grant 2.1.1.3483 of the Federal Agency of Education of the Russian Federation, and by the grant MK-405.2010.2 of the President of the Russian Federation.

---

1. N. V. Nabokov and Yu. V. Baryshev, in *Proceedings of the International Conference "Problems of Practical Cosmology"*, S-Peterburg, Russia, 2008 (Rus. Geograph. Society, S-Peterburg, 2008), V. 2, p. 69.
2. N. V. Nabokov and Yu. V. Baryshev, Astrofizika **53**, 105 (2010).
3. N. V. Nabokov and Yu. V. Baryshev, Astrofizika **53**, 117 (2010).
4. V. V. Sokolov, S. V. Zharikov, Yu. V. Baryshev, et al., Astronom. and Astrophys. **344**, 43 (1999).
5. T. A. Fatkhullin, A. A. Vasilyev and V. P. Reshetnikov, Pis'ma Astronom. Zh. **30**, 323 (2004).
6. A. S. Moskvitin, E. Sonbas, I. V. Sokolov, and T. A. Fatkhullin, in *Proceedings of the International Conference "Problems of Practical Cosmology"*, S-Peterburg, Russia, 2008 (Rus. Geograph. Society, S-Peterburg, 2008), V. 2, p. 228.
7. T. A. Fatkhullin, Candidate's Dissertation in Mathematics and Physics, (SAO RAS, Nizhnii Arkhyz, 2003).
8. V. V. Sokolov, T. A. Fatkhullin, V. N. Komarova, and A. V. Moiseev, GCN 1717 (2002).
9. A. de Ugarte Postigo et al., Astronom. and Astrophys. **443**, 841 (2005).
10. D. W. Fox, GCN 1564 (2002).
11. "SCORPIO: Spectral Camera with Optical Reducer for Photometrical and Interferometrical Observations" `http://www.sao.ru/ moisav/scorpio/ /scorpio.html`.
12. M. S. Bessell, Publ. Astronom. Soc. Pacific **102**, 1181 (1990).
13. "USNO Flagstaff station: Integrated Image and Catalogue Archive Service" `http://www.nofs.navy.mil/data/FchPix/`.
14. E. Bertin and S. Arnouts, Astronom. and Astrophys. Suppl. Ser. **117**, 393 (1996).
15. R. G. Kron, Astrophys. J. Suppl. **43**, 305 (1980).
16. S. I. Neizvestny, Izv. Spec. Astroph. Obs. **17**, 26 (1983).
17. Arne A. Henden, GCN 1583 (2002).
18. M. Bolzonella, J.-M. Miralles, and R. Pelló, Astronom. and Astrophys. **363**, 476-492 (2000).
19. D. J. Schlegel, D. P. Finkbeiner, and M. Davis, Astrophys. J. **500**, 525 (1998).